Heliyon 8 (2022) e10122

Contents lists available at ScienceDirect

Heliyon

journal homepage: www.cell.com/heliyon

Research article

Exploring flexibility, intermolecular interactions and ADMET profiles of anti-influenza agent isorhapontigenin: A quantum chemical and molecular docking study

Sathya Bangaru [a,b], Govindammal Madhu [a], M. Srinivasan [b], Prasath Manivannan [a,*]

[a] Department of Physics, Periyar University PG Extension Centre, Dharmapuri, 636 701, Tamilnadu, India
[b] SSN Research Centre, SSN College of Engineering, Kalavakkam, Chennai, 603 110, Tamilnadu, India

ARTICLE INFO

Keywords:
Influenza
FT-IR
FT-Raman
UV-Vis
ADMET

ABSTRACT

Isorhapontigenin (IRPG) drug emerges as promising efficient inhibitor for H1N1 and H3N2 subtypes which belong to influenza A virus; reported with IC_{50} value of 35.62 and 63.50 μM respectively. When experimental data are compared to the predicted geometrical parameters and vibrational assignments (FT-IR and FT-Raman), the findings indicated a strong correlation. The absorption bands of π→π* transitions are revealed through UV-Vis electronic properties; this confirms that the IRPG molecule shows strong bands. Through NBO and HOMO-LUMO analysis, the kinetic stability and chemical reactivity of the IRPG molecule were investigated. By using an MEP map, the IRPG's electrophilic and nucleophilic site selectivity was assessed. In a molecular docking investigation, the IRPG molecule shows a stronger inhibition constant and binding affinity for the H1N1 and H3N2 influenza virus. The IRPG molecule thus reveals good biological actions in nature and can be used as a potential therapeutic drug candidate for H1N1 and H3N2 virus A influenza.

1. Introduction

Since overall scourge strains and yearly pandemic, Influenza can cause an intense respiratory ailment [1] caused by RNA virus which belongs to the Orthomyxoviridae family [2]. As the mortality and morbidity rate caused by influenza virus is very high, it crafts severe consequences throughout the world [3, 4, 5, 6, 7, 8]. Influenza contains two glycoproteins specially; Hemagglutinin (HA) [9] and Neuraminidase (NA) [10] based on this influenza A is branched into subgroups. Consequently, H1N1 and H3N2 subtypes are endemic in humans, while HA has 18 subgroups and NA has 11 subgroups [11, 12]. HA was a cell-anchoring viral glycoprotein that links monosaccharide sialic acid, which has receptors on the host cells, and causes viral infection by facilitating the entry and fusion of virus [13]. A hydrolytic viral glycoprotein known as NA (sialidase) is capable of cleaving sialic acid off cell surfaces as well as releasing progeny virus particles from host cells [14]. Hence the viral NA enzyme has been a functioning exploration territory against anti-influenza treatment due to release of virus particles from host cells. For the vast majority, influenza settles on its own, but in some cases its complications can be treacherous. In this sense there is a need of proceeding requirement for advancement of new anti-influenza drugs.

The majority of research researchers are currently making less generic antiviral medicines derived from plants to fight influenza viruses. Isorhapontigenin (IRPG) is an isomer of rhapontigenin derived from Chinese herb *Gnetum cleistostachyum* [15] which belongs to the family *Gnetaceae* and also from some wine grapes. Gnetum species were recognized to hold oligomers of IRPG. The IRPG possess stilbenoid structure with four hydroxyl groups and one methoxy group attached to it. IRPG has various biological effects like anti-oxidative, anti-cancer, anti-HIV, anti-fungal, protein kinase C inhibitory, anti-inflammatory and cytotoxic activities [16]. IRPG was recognized as an inhibitor of influenza A virus which has subgroups H1N1 and H3N2. According to research, IRPG targets have IC50 values of 35.62 μM for H1N1 NA enzyme inhibition and 63.50 μM for H3N2 NA enzyme inhibition [17].

As IRPG has extraordinary pharmaceutical application in treating influenza, an endeavor has been made to examine its molecular properties. A complete literature survey has been done and it is found that so far either spectroscopic investigations or molecular docking studies have not been reported. In HF (Hartree-Fock) method electron correlation is excluded, thus it will be difficult to ascertain certain properties of the drugs. Hence this research investigation has been executed through DFT/B3LYP method with 6-311G(d,p) basis set to study various spectroscopic

* Corresponding author.
E-mail address: sanprasath2006@gmail.com (P. Manivannan).

https://doi.org/10.1016/j.heliyon.2022.e10122
Received 5 November 2021; Received in revised form 7 January 2022; Accepted 25 July 2022

and biological properties of IRPG. The calculated spectroscopic data (FT-IR and FT-Raman) supported via potential energy distribution were compared with experimentally recorded values. Electronic (UV-Vis) spectral analysis was recorded and compared with theoretically predicted spectra computed through TD-DFT method. Global reactivity descriptors were determined with the help of frontier molecular energies. The reactive sites and electronic structure of the molecule was determined by MEP map and NBO respectively. A molecular docking, drug-likeness and ADMET predictions are used to analyze the drug behavior in nature and active site cavity of NA. The development of drugs depends heavily on actual research in order to analyze potential drug candidates for antiviral agents against the H1N1 and H3N2 influenza viral epidemic.

2. Procedure

2.1. Experimental details

The compound IRPG was purchased from the Tokyo Chemical Industry (TCI) chemical firm (purity of >95.0 percent) and used for the spectral measurements without any additional purification. Utilizing KBr pellet method, an FT-IR spectrometer (Bruker Tensor 27) was used to trace the IRPG's FT-IR spectra in the 400–4000 cm-1 (4 cm-1 resolution) region. The FT-Raman spectra of the IRPG in the range of 400–4000 cm-1 was traced using a Bruker RFS 27 FT-Raman Spectrophotometer (1064 nm Nd: YAG laser source). A UV-vis spectrophotometer (UV-2501, Shimadzu Corp., Japan) has been used to record the ultraviolet-visible-NIR (UV-vis-NIR) spectra of the IRPG in an array between 200 and 900 nm.

2.2. Computational details

The DFT approach was used to optimize the IRPG molecule using the Gaussian09W software suite [18]. IRPG geometrical aspects have been conquered via Gauss view 5.0 software [19]. Using VEDA 4xx program package [20] the vibrational assignments for IRPG was requiring through an average of potential energy distribution percentage (PED %). Moreover, WinXPRO software [21] was used to create the MEP map of the IRPG molecule from the potential cube file created by Gaussian09W program. Furthermore, the IRPG molecule's electronic characteristics (UV absorbance, HOMO, and LUMO) were identified using the TD-DFT approach [22, 23, 24] carried out using Gaussian 09W software [18]. NBO 3.1 program was used to compute the second order Fock matrix, which controls how the IRPG interacts with its donors and acceptors [25]. The AutoDock4.2 software package [26] was used to carry out the molecular docking exploration, and the software programmes such as Discovery Studio [27], Chimera [28], PyMOL [29] and Ligplot [30] were used to investigate the interactions between the IRPG ligand molecule and the NA enzyme.

3. Result and discussion

Recently, the machine learning is gaining fame in biomaterial and computational field. Machine learning will be handy and fast method. On comparing with experimental method, computational method is less cost effective without wasting chemicals and less time for material development [31, 32, 33]. The main benefit of utilizing DFT techniques is a

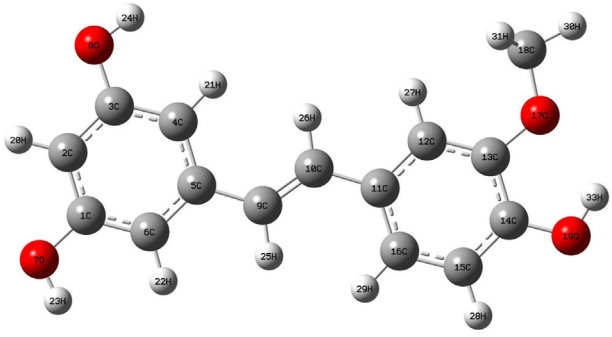

Figure 1. The ball and stick model of optimized structure of IRPG with atom numbering scheme.

Table 1. Selected bond lengths and bond angles of IRPG molecule compared with XRD data.

Bond length (Å)	Calculated[b]	Exp[a] values	Bond angle (°)	Calculated[b]	Exp[a] values
C(1)–C(2)	1.391	1.387	C(2)–C(1)–C(6)	120.7	121.1
C(1)–C(6)	1.396	1.388	C(2)–C(1)–O(7)	117.1	116.6
C(1)–O(7)	1.366	1.378	C(6)–C(1)–O(7)	122.2	122.3
C(2)–C(3)	1.395	1.390	C(1)–C(2)–C(3)	118.7	118.5
C(2)–H(20)	1.082	0.950	C(1)–C(2)–H(20)	120.7	120.8
C(3)–C(4)	1.393	1.383	C(3)–C(2)–H(20)	120.5	120.8
C(3)–O(8)	1.367	1.374	C(2)–C(3)–C(4)	121.2	121.6
C(4)–C(5)	1.404	1.401	C(2)–C(3)–O(8)	116.6	116.8
C(4)–H(21)	1.085	0.950	C(4)–C(3)–O(8)	122.2	121.6
C(5)–C(6)	1.403	1.398	C(3)–C(4)–C(5)	120.2	119.7
C(5)–C(9)	1.465	1.471	C(3)–C(4)–H(21)	119.2	120.1
C(6)–H(22)	1.086	0.950	C(5)–C(4)–H(21)	120.6	120.1
O(7)–H(23)	0.963	0.920	C(4)–C(5)–C(6)	118.5	119.1
O(8)–H(24)	0.963	0.900	C(4)–C(5)–C(9)	123.3	121.9
C(9)–C(10)	1.345	1.338	C(6)–C(5)–C(9)	118.1	119.0
C(9)–H(25)	1.087	0.950	C(1)–C(6)–C(5)	120.6	120.1
C(10)–C(11)	1.463	1.462	C(1)–C(6)–H(22)	119.8	120.0
C(10)–H(26)	1.087	0.950	C(5)–C(6)–H(22)	119.5	120.0
C(11–C(12)	1.411	1.400	C(1)–O(7)–H(23)	109.1	110.4
C(11)–C(16)	1.402	1.406	C(3)–O(8)–H(24)	109.1	112.2
C(12)–C(13)	1.386	1.385	C(5)–C(9)–C(10)	127.1	126.0
C(12)–H(27)	1.083	0.950	C(5)–C(9)–H(25)	114.2	117.0
C(13)–C(14)	1.407	1.386	C(10)–C(9)–H(25)	118.7	117.0
C(13)–O(17)	1.374	-	C(9)–C(10)–C(11)	127.4	128.2
C(14)–C(15)	1.390	1.390	C(9)–C(10)–H(26)	118.4	115.9
C(14)–O(19)	1.359	1.381	C(11)–C(10)–H(26)	114.1	115.9
C(15)–C(16)	1.390	1.382	C(10)–C(11)–C(12)	118.3	118.9
C(15)–H(28)	1.083	0.950	C(10)–C(11)–C(16)	123.8	123.7
C(16)–H(29)	1.083	0.950	C(12)–C(11)–C(16)	117.9	117.4
O(17)–C(18)	1.421	-	C(11)–C(12)–C(13)	121.0	122.0
C(18)–H(30)	1.089	-	C(11)–C(12)–H(27)	118.8	119.0
C(18)–H(31)	1.095	-	C(13)–C(12)–H(27)	120.1	119.0
C(18)–H(32)	1.095	-	C(12)–C(13)–C(14)	120.2	119.2
O(19)–H(33)	0.967	0.880	C(12)–C(13)–O(17)	126.2	-
			C(14)–C(13)–O(17)	113.6	-
			C(13)–C(14)–C(15)	119.2	120.3
			C(13)–C(14)–O(19)	120.4	118.1
			C(15)–C(14)–O(19)	120.4	121.6
			C(14)–C(15)–C(16)	120.5	120.0
			C(14)–C(15)–H(28)	118.3	120.0
			C(16)–C(15)–H(28)	121.2	120.0
			C(11)–C(16)–C(15)	121.2	121.1
			C(11)–C(16)–H(29)	120.2	119.5
			C(15)–C(16)–H(29)	118.6	119.5
			C(13)–O(17)–C(18)	118.5	-
			O(17)–C(18)–H(30)	106.1	-
			O(17)–C(18)–H(31)	111.2	-
			O(17)–C(18)–H(32)	111.2	-
			H(30)–C(18)–H(31)	109.4	-
			H(30)–C(18)–H(32)	109.4	-
			H(31)–C(18)–H(32)	109.5	-
			C(14)–O(19)–H(33)	107.2	109.7

[a] Experimental values taken from Ref.[**32**]. Calculated[a] for 6-311G(d,p) basis sets.

Table 2. The observed (FT-IR and FT-Raman) and computed vibrational frequencies using DFT for IRPG.

Species	Observed Wavenumbers (cm^{-1})		Computed Wavenumbers (cm^{-1}) B3LYP/6-311G(d,p)						Vibrational Assignments
	FT-IR	FT-RAMAN	unscaled frequency	scaled frequency	IR-intensities		Raman-intensities		
					Abs	Rel	Abs	Rel	
W(93)			3835	3708	36	13	142	3	νOH(96)
W(92)			3834	3707	62	23	46	1	νOH(96)
W(91)	$3367_{(s,b)}$		3773	3648	163	59	208	5	νOH(100)
W(90)			3211	3105	0	0	171	4	νCH(100)
W(89)			3198	3092	8	3	145	3	νH(98)
W(88)			3187	3082	9	3	36	1	νCH(97)
W(87)		$3071_{(w)}$	3183	3078	6	2	65	1	νCH(97)
W(86)			3165	3061	12	4	35	1	νCH(97)
W(85)			3150	3046	29	10	69	2	νCH(95)
W(84)			3144	3040	14	5	5	0	νCH(99)
W(83)			3136	3033	26	10	171	4	νCH(91)
W(82)	$3020_{(s)}$		3134	3030	4	1	24	1	νCH(97)
W(81)			3067	2966	37	14	45	1	νCH(100)
W(80)	$2937_{(m)}$		3007	2908	44	16	135	3	νCH(92)
W(79)		$1635_{(s)}$	1689	1633	9	3	3285	74	νCC(50)+δHCC(21)
W(78)	$1607_{(m)}$		1650	1595	9	3	99	2	νCC(43)
W(77)		$1594_{(s)}$	1647	1593	170	62	302	7	νCC(39)
W(76)			1641	1587	126	46	1480	33	νCC(29)
W(75)			1628	1574	229	84	4458	100	νCC(28)
W(74)			1551	1500	274	100	2	0	δHCC(11)
W(73)	$1520_{(s)}$		1546	1495	39	14	224	5	δHCC(11)
W(72)	$1454_{(m)}$		1508	1458	65	24	8	0	δHCH(68)+τHCOC(20)
W(71)			1490	1441	9	3	18	0	δHCH(76)+τHCOC(16)
W(70)			1488	1439	62	23	79	2	δHCH(40)
W(69)			1482	1433	99	36	87	2	δHCH(22)
W(68)			1460	1412	7	3	208	5	νCC(20)
W(67)	$1373_{(m)}$		1412	1365	48	17	235	5	νCC(29)+δHCC(11)+δHOC(29)
W(66)		$1345_{(s)}$	1383	1337	60	22	5	0	νCC(30)
W(65)			1374	1329	134	49	548	12	νCC(16)+νOC(20)
W(64)		$1309_{(s)}$	1356	1311	17	6	604	14	νCC(20)+δHCC(58)
W(63)		$1294_{(s)}$	1335	1291	12	5	22	1	δHCC(36)
W(62)	$1285_{(s)}$		1327	1283	50	18	104	2	δHCC(21)
W(61)			1310	1267	237	87	273	6	νOC(16)+νCC(19)+δHCC(10)
W(60)			1293	1250	172	63	89	2	νOC(19)+δHCC(14)
W(59)	$1217_{(s)}$	$1215_{(w)}$	1258	1216	73	27	95	2	δHCC(11)
W(58)			1233	1192	84	30	238	5	νCC(12)+δHCC(28)+δHOC(22)
W(57)			1224	1183	37	13	16	0	νCC(10)+δHCC(12)+δHOC(23)
W(56)			1221	1181	131	48	3	0	δHOC(55)
W(55)			1213	1173	66	24	43	1	δHOC(13)+τHCOC(24)
W(54)	$1155_{(s)}$	$1160_{(s)}$	1193	1153	58	21	239	5	δHCC(20)+τHCOC(20)
W(53)		$1148_{(s)}$	1176	1137	25	9	1017	23	νCC(10)+δHCC(12)
W(52)			1173	1134	1	0	3	0	δHCH(28)+τHCOC(72)
W(51)		$1120_{(w)}$	1154	1116	224	82	9	0	νOC(27)+δHCC(45)
W(50)			1146	1109	41	15	147	3	δCCC(11)+δHCC(39)
W(49)	$1015_{(s)}$	$1010_{(w)}$	1061	1026	47	17	14	0	νOC(54)+δCCC(32)
W(48)		$996_{(s)}$	1028	994	32	12	50	1	νCC(18)+νOC(16)+δCCC(11)
W(47)			1012	978	47	17	13	0	νCC(22)+νOC(19)
W(46)			1006	973	2	1	175	4	νCC(39)+δCCC(45)
W(45)	$949_{(s)}$	$954_{(m)}$	988	955	42	15	0	0	τHCCC(86)
W(44)			948	917	5	2	4	0	νCC(22)+νOC(11)+δCCC(10)
W(43)			937	906	5	2	1	0	τHCCC(78)+τCCCC(14)
W(42)	$839_{(s)}$		887	857	3	1	21	0	τHCCC(76)+τCCCC(10)
W(41)			848	820	15	6	4	0	τHCCC(54)
W(40)		$805_{(m)}$	831	803	15	6	1	0	τHCCC(60)
W(39)			824	797	30	11	2	0	τHCCC(79)

(*continued on next page*)

Table 2 (*continued*)

Species	Observed Wavenumbers (cm^{-1})		Computed Wavenumbers (cm^{-1}) B3LYP/6-311G(d,p)						Vibrational Assignments
	FT-IR	FT-RAMAN	unscaled frequency	scaled frequency	IR-intensities		Raman-intensities		
					Abs	Rel	Abs	Rel	
W(38)		$781_{(m)}$	820	793	20	7	53	1	νCC(16)+νOC(23)
W(37)			797	770	1	0	1	0	τHCCC(68)+γOCCC(10)
W(36)			795	769	19	7	19	0	νCC(21)+νOC(13)
W(35)			774	748	41	15	0	0	τHCCC(57)+γOCCC(10)
W(34)	$679_{(s)}$		714	690	1	0	1	0	τHCCC(10)+τCCCC(49)+γOCCC(32)
W(33)			688	665	5	2	4	0	δCCC(14)
W(32)			677	655	18	7	0	0	τHCCC(30)+τCCCC(42)
W(31)	$625_{(w)}$		634	613	7	3	0	0	τHCCC(10)+τCCCC(11)+γOCCC(22)
W(30)			620	599	0	0	0	0	τHCCC(21)+γOCCC(67)
W(29)	$573_{(s)}$		584	565	5	2	9	0	δCCC(10)+δHCC(12)
W(28)			579	560	0	0	0	0	τCCCC(22)+γCCCC(19)
W(27)			577	558	29	11	4	0	δOCC(12)
W(26)			555	537	10	4	4	0	δOCC(34)
W(25)			535	517	7	2	6	0	δCCC(13)
W(24)			521	504	11	4	5	0	δCCC(68)
W(23)			496	480	18	6	1	0	νOC(10)+δCCC(30)+δCOC(16)
W(22)	$461_{(w)}$		475	459	60	22	4	0	τHOCC(66)+γOCCC(11)
W(21)			450	435	46	17	0	0	τHOCC(29)+τCCCC(29)+γOCCC(14)
W(20)			415	402	1	0	1	0	δCCC(30)+δCOC(15)
W(19)			377	365	0	0	2	0	τCCCC(44)+γOCCC(32)
W(18)			344	332	19	7	5	0	τHOCC(95)
W(17)			341	330	2	1	1	0	δOCC(66)
W(16)			336	325	179	65	1	0	δOCC(48)+δCOC(15)+τHOCC(95)
W(15)			336	324	14	5	3	0	δOCC(48)+δCOC(15)+τHOCC(95)
W(14)			291	281	0	0	1	0	τHCOC(13)+τCCCC(23)+γOCCC(16)
W(13)		$246_{(w)}$	253	245	3	1	1	0	δOCC(32)+δCOC(14)+δCCC(12)
W(12)			251	243	2	1	2	0	τHCOC(10)+τCCCC(27)
W(11)		$230_{(w)}$	234	226	0	0	2	0	τCCCC(74)
W(10)		$204_{(w)}$	220	212	7	2	2	0	τCCCC(30)+γOCCC(35)
W(9)			198	191	0	0	0	0	τCCCC(24)+γOCCC(11)
W(8)		$179_{(w)}$	178	172	0	0	3	0	νCC(24)+δCCC(15)+δOCC(14)
W(7)			159	154	0	0	4	0	τCCCC(52)
W(6)		$95_{(s)}$	157	152	1	0	4	0	δOCC(15)+δCCC(48)
W(5)		$71_{(s)}$	77	75	4	1	1	0	τCOCC(77)+τHCOC(10)
W(4)			65	62	0	0	1	0	τCCCC(63)
W(3)			52	50	0	0	0	0	δCCC(100)
W(2)			45	44	0	0	0	0	τCCCC(72)+γCCCC(14)
W(1)			8	8	0	0	0	0	τCCCC(91)

m = medium, w = weak, s = strong, n = narrow, b = broad, sh = sharp, ν-stretching; δ-bending, γ-out of plane torsion; τ-torsion.

significant expansion in computational precision without increase in the computational time. As a results, the research is based on DFT level of theory based on machine learning.

3.1. Geometry analysis

Geometrical properties like bond lengths and bond angles of IRPG molecule is calculated with 1DFT (B3LYP level of theory) method [34, 35] through basis sets (6-311G(d,p)) and the optimized scaled ball and stick model is shown in Figure 1. IRPG molecule was converged at the threshold limits of maximum force (0.000023 a.u.) and displacement (0.001240 a.u.) whereas the gradient of potential energy surface was converged with the RMS gradient value (0.000307 a.u.), and also the dipole moment value was 2.2865 Debye. The computed structural parameters of IRPG molecule were related through experimental XRD data [36] correlated to the structure because IRPG crystal structure is not published so far based on literature survey and the parameter values are represented in Table 1. Because computed values are analysed in gas phase whereas experimental values are analysed in solid phase, there is a small difference between the experimental and computed values for the IRPG molecule. In IRPG molecule, the resorcinol ring C–C bond lengths ranges from 1.366 to 1.407 Å. The hydroxyl groups (O–H) present in resorcinol ring is O(8)–H(24) and O(7)–H(23) the values are found to be 0.966/0.963/0.900* Å and 0.966/0.963/0.920* Å respectively (* specifies the experimental value). The hydroxyl group present in 2^{nd} ring is O(19)–H(33) and the value is 0.970/0.967/0.880* Å. In the bond angles, C(5)–C(9)–C(10) and C(9)–C(10)–C(11) are the highest bond angles values present in IRPG molecule. The C-C homonuclear bond length correlates to repellent due to identical charges, but the C-H, C-O, and O-H hetronuclear bond lengths correlate to attractive due to opposite charges. Moreover, the hetronuclear is smaller when compare to homonuclear bonds [37]. These geometrical data therefore, provide a good estimate with experimental crystal data, and the values are suitable enough for computing vibrational frequencies.

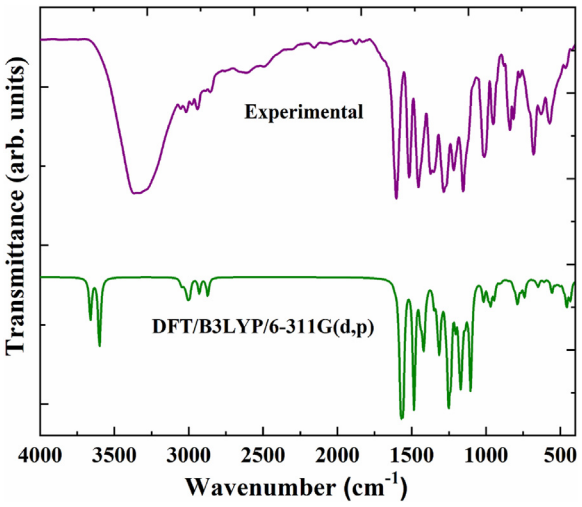

Figure 2. Experimental (Violet) and theoretical (Green-B3LYP/6-311G(d,p)) FT-IR spectra of IRPG.

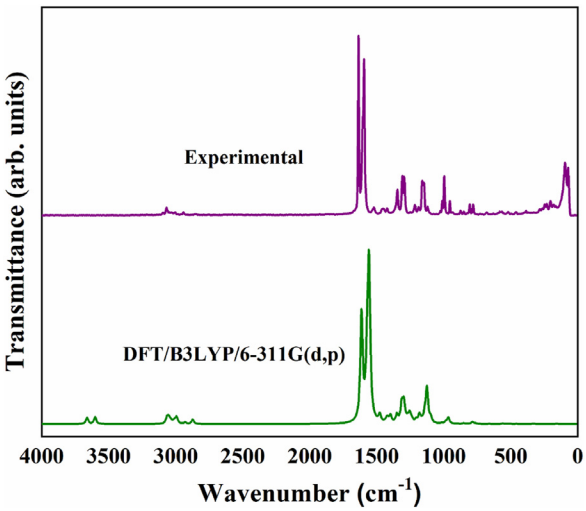

Figure 3. Experimental (Violet) and theoretical (Green-B3LYP/6-311G(d,p)) FT-Raman spectra of IRPG.

3.2. Vibrational frequency analysis

In order to evaluate the calculated vibrational frequencies (FT-IR and FT-Raman) for the IRPG molecule, DFT was used. The basis sets used were 6-311G(d,p), which were scaled down by scaling factors (0.961 and 0.967) [38] and its PED percent was examined using the VEDA 4xx software [20]. The values are in excellent agreement with the basis set 6-311G(d,p) when the experimental data are compared to theoretically calculated data. This is due to the allocation of Gaussian type orbitals (GTOs) for absolutely describing the H, O, and C atoms. The more stable C1 point symmetry group and 33 atoms with 93 vibrational modes are both features of the IRPG molecule. Table 2 represents the IR intensities, Raman intensities, vibrational assignments for IRPG. Figures 2 and 3 display the observed and predicted FT-IR and FT-Raman spectra for IRPG molecule. Sathya et al [48, 49, 50, 51] also reported this type of plant derivative molecule as this type of value difference because the DFT calculations are taken from gas phase and experimental values are observed from solid phase.

3.2.1. Hydroxyl (O–H) vibrations

The O–H stretching vibrations are extremely sensitive and reveals wide range in intensity, bandwidth, and wavenumber due to intra or intermolecular hydrogen bonding in the molecule. O–H stretching vibrations commonly occur in the region and also Bhavani et al [39] also reported the region of 3600–3200 cm^{-1} (while H-bonded) and 3700-3500 cm^{-1} (while stretch free) [39, 40]. In IRPG molecule the theoretical wavelength are observed at 3708, 3707 and 3648 cm^{-1} for 6-311G(d,p) by a PED contributions of 96, 96 and 100 % respectively. Experimental values for IRPG molecule were detected at 3367 cm^{-1} in FT-IR due to solid phase the large difference is present.

3.2.2. C–H vibrations

The vibrations of C–H frequently occurs between the region from 3100 to 3000 cm^{-1} for strong Raman peaks [41]. In IRPG molecule the vibrations occur in the region of 3105, 3092, 3082, 3078, 3061, 3046, 3040, 3033, 3030, 2966, 2908 cm^{-1} for 6-311G(d,p). The experimental values are detected at 3020, 2937 cm^{-1} for FT-IR and 3071 cm^{-1} for FT-Raman. The analysed theoretical 6-311G(d,p) values and the experimental ones are in good agreement.

3.2.3. Carbonyl (C–O) vibrations

The C=O stretch in ketones, which is calculated to be in the range of 1740–1660 cm^{-1} [42], matches the COOH group's C=O stretching vibration precisely. Generally, the C-O stretching vibrations can be predicted between 1300 and 1000 cm^{-1} [43]. In IRPG molecule C–O stretching vibrations appears in the region of 1015 cm^{-1} for FT-IR and 1120, 1010, 996 cm^{-1} for FT-Raman. The analysed values are observed in the region of 1116, 1026, 994, 978, 917 cm^{-1} for 6-311G(d,p).

3.2.4. C–C vibrations

In the region of 1650–1400 cm^{-1} [44], C–C vibrational bands promote the aromatic and hetero aromatic modes, while in the range of 1300–1000 cm^{-1} [45], C-C ring stretching vibrations are predicted. The C–C vibrations are reported at 1635, 1594, 1345, 1309, 1148, 781 cm^{-1} in FT-Raman and 1607, 1373 cm^{-1} in FT-IR for IRPG molecule. The predicted values are observed in the range of 633–793 cm^{-1} in 6-311G(d,p).

3.3. Molecular electrostatic potential (MEP)

The necessary characteristics of drugs and biomolecules, such as electron density, reactivity, electrophilic and nucleophilic sites, as well as the H bonding interaction between the NA enzyme and the IRPG, are clearly explained by the MEP map. Likewise, the positive area of the MEP map contributes to electrophilic sites (which resemble regions with higher electron densities), while the negative region contributes to nucleophilic sites (resembles to lower electron density) [46, 47, 48]. The Mulliken sketch and the MEP as shown in Figure 4 are identical, and the MEP map for IRPG is coloured based on Mulliken atomic charges. Furthermore, the increasing electron density order of red<orange<yellow<green<sky-blue<blue denotes the nucleophilic and electrophilic sites for IRPG. The MEP map colour code for IRPG molecule is in the range among -6.225 × 10^{-2} (orange and

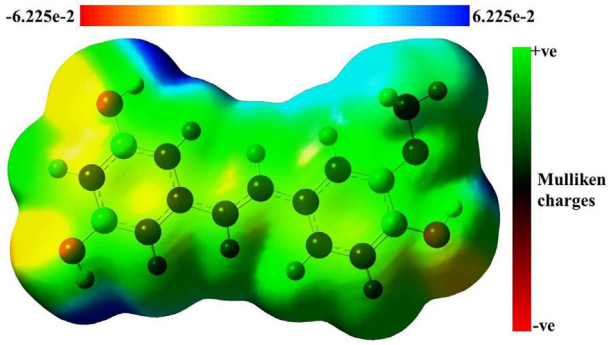

Figure 4. Molecular electrostatic potential map of IRPG coloured on the basis of Mulliken atomic charges.

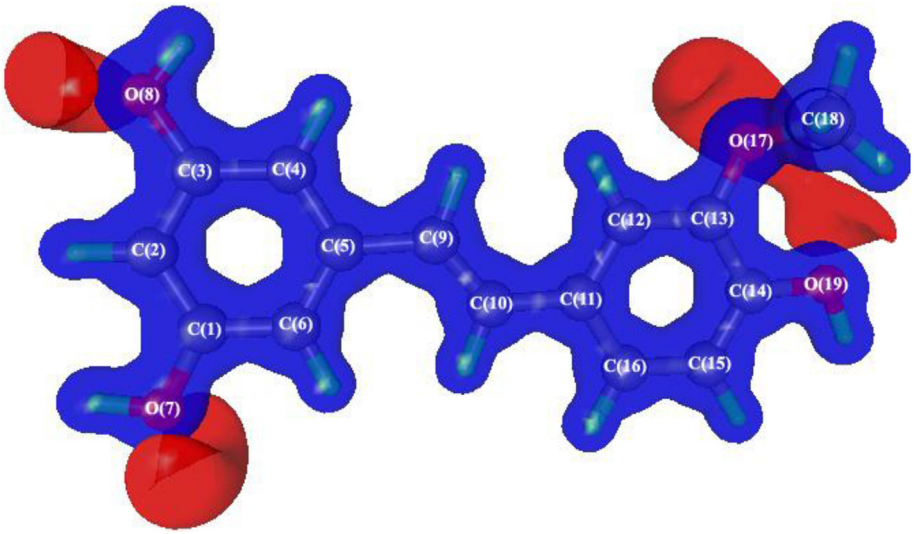

Figure 5. Molecular electrostatic potential map of IRPG molecule showing the electropositive (blue) and electronegative (red) regions of the molecule, the Iso surface values are positive potential at 0.8eÅ^{-1} and negative potential at 0.08eÅ^{-1}.

Table 3. Electronic properties of IRPG calculated using TD-DFT (B3LYP)/6-311G(d,p).

Experimental		TD-DFT (B3LYP)/6-311G(d,p)				
λ_{max} (nm)	Energy (eV)	λ_{cal} (nm)	Energy (eV)	Oscillating strength F	Assignments for major transitions	Major contributions (>10%)
333	3.7233	349	3.5489	1.0274	$\pi \rightarrow \pi^*$	HOMO->LUMO (100%)
307	4.0386	311	3.9875	0.037	$\pi \rightarrow \pi^*$	H-1->LUMO (94%)
282	4.3966	288	4.2965	0.0687	$\pi \rightarrow \pi^*$	H-2->LUMO (67%), HOMO->L+1 (22%)

deepest red) to 6.225 × 10^{-2} (sky blue and deepest blue). Green colour signifies neutral charge, whereas orange to deepest red colour denotes positive electrostatic potential, sky blue to deepest blue colour indicates negative electrostatic potential for the IRPG molecule. The values of the IRPG molecule iso surface representation in Figure 5 are positive potential at 0.8 eÅ^{-1} and negative potential at 0.08 eÅ^{-1}. While the O atom has red colour (nucleophilic area), the H and C atoms have blue colour (electrophilic area). The O(7), O(8), O(17), and O(19) atoms in the IRPG molecule have the most negative regions, and these O atoms from the Mulliken sketch similarly have negative regions. Evidently, the MEP and Mulliken charges are parallel, as shown by the pictorial representation.

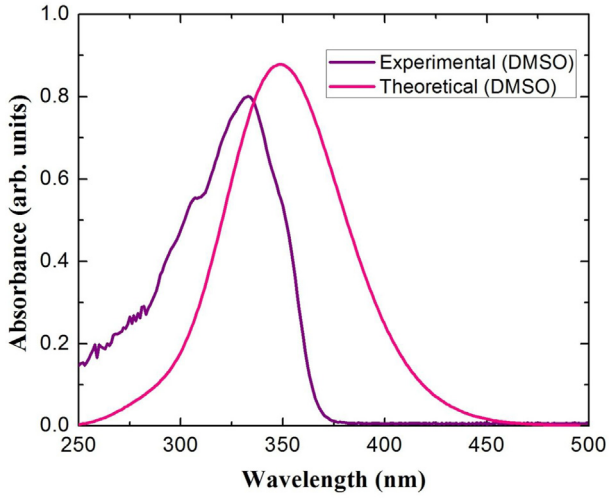

Figure 6. Experimental and theoretical absorption spectra of IRPG in DMSO solution.

3.4. Electronic transition analysis

Through the UV-Vis absorption spectra, the nature of the electronic transition properties for the IRPG molecule was examined. This transition occurs from the HOMO to LUMO level and was absorbed by bonding (π, σ), anti-bonding (π*, σ*), and non-bonding (n). The theoretical spectrum of the IRPG molecule was calculated using the TD-DFT method (6-311G(d,p) basis set) with DMSO as a solvent and the results are compared to those obtained experimentally. Table 3 exposes the electronic parameters of IRPG molecule. The IRPG molecule's experimental and analytical spectra are shown in Figure 6. Through UV absorption bands of the π→π* and n→π* transitions, the existence of the strong and weak bands were validated [49, 50, 51, 52]. The π→π* electronic transition bands of IRPG molecule was experimentally observed at 333, 307 and 282 nm and theoretically observed at 349, 311 and 288 nm, these values are closely reliable with each other. Subsequently, this transition clearly says about the strong interaction among IRPG and DMSO solvent which reveals the biological character of the IRPG drug.

3.5. Global reactivity descriptors

Through the use of HOMO and LUMO energies, the kinetic stability, chemical reactivity, and toxicity of the drug molecule are evaluated. LUMO energy exhibit nucleophilic behaviour (electron acceptance), while HOMO energy exhibits electrophilic behaviour (electron donation). The global reactivity descriptors such as ionization potential ($I = -E_{HOMO}$), electron affinity ($A = -E_{LUMO}$), global hardness ($\eta = (I-A)/2$), chemical softness ($s = 1/2\eta$), electronegativity ($\chi = (I + A)/2$), chemical

Table 4. Calculated global reactivity descriptors for IRPG.

Molecular descriptors Energy(eV)	IRPG (eV)
HOMO energy (E_{HOMO})	-5.368
LUMO energy (E_{LUMO})	-1.508
Band gap (Eg)	3.859
Ionization potential (I)	5.368
Electron affinity (A)	1.508
Global hardness (η)	1.929
Chemical softness (s)	0.259
Electronegativity (χ)	3.438
Chemical potential (μ)	-3.438
Electrophilicity (ω)	3.062

potential ($\mu = -\chi$) and electrophilicity ($\omega = \mu^2/2\eta$) were computed for IRPG molecule and listed in Table 4. The global reactivity descriptors of IRPG molecule is revealed in Figure 7.

Band gap energy refers to the energy differential between the molecular orbitals (HOMO and LUMO), where a large band gap energy indicates a hard molecule and a small band gap energy indicates a soft molecule [44, 49, 50, 51, 52]. Since the IRPG molecule's band gap energy is observed to be 3.859 eV, it can be presumed that the molecule is a soft one. The Koopmans's theorem [53] for closed-shell molecules asserts that the molecule's ionization potential and electron affinity are related to how much energy a system changes when an electron is removed or added. The negative of HOMO and LUMO energy are ionization potential (5.368 eV) and electron affinity (1.508 eV) respectively. In order to calculate the electron density of the molecule, Pauling and Mulliken [54, 55, 56] describe the electronegativity (measure the propensity to attract electrons through an atom in a covalent bridge) and the value is determined to be 3.438 eV. When compared to electron affinity and

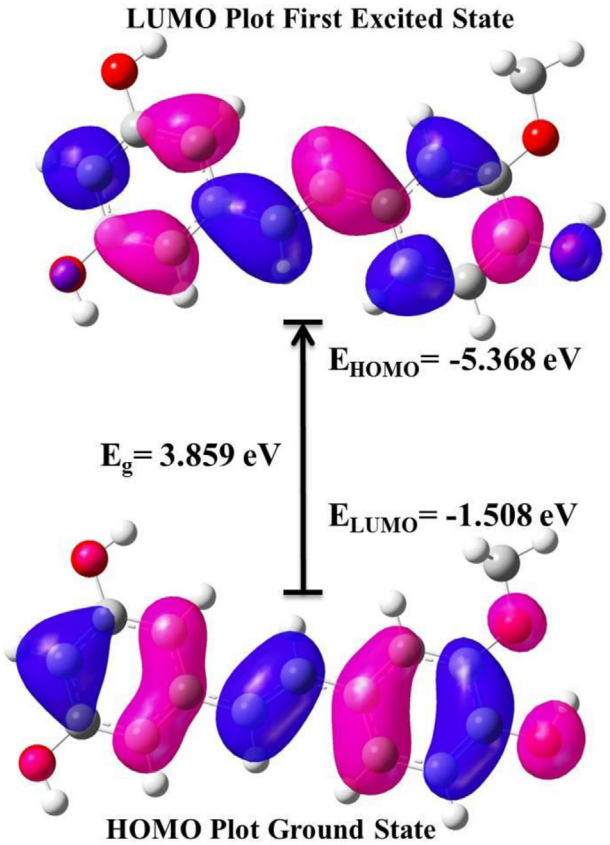

Figure 7. The HOMO and LUMO orbitals of IRPG.

Table 5. The natural bond energy values of IRPG at 6-311G(d,p) level of theory.

Donor (i)	ED (e)	Acceptor (j)	ED (e)	E(2)[a] (kJ mol^{-1})	E(j)-E(i)[b] (a.u)	F(i, j)[c] (a.u)
π(C1 –C2)	1.667	π*(C3–C4)	0.397	26.36	0.28	0.08
π(C1–C2)	1.667	π*(C5–C6)	0.421	14.98	0.29	0.06
π(C3–C4)	1.685	π*(C1–C2)	0.392	13.94	0.29	0.06
π(C3–C4)	1.685	π*(C5–C6)	0.421	24.73	0.29	0.08
π(C5–C6)	1.678	π*(C1–C2)	0.392	26.28	0.28	0.08
π(C5–C6)	1.678	π*(C3–C4)	0.397	13.89	0.28	0.06
π(C5–C6)	1.678	π*(C9–C10)	0.146	14.02	0.30	0.06
π(C9–C10)	1.868	π*(C5–C6)	0.421	13.99	0.30	0.06
π(C9–C10)	1.868	π*(C11–C16)	0.403	11.69	0.30	0.06
π(C11–C16)	1.645	π*(C9–C10)	0.146	12.77	0.30	0.06
π(C11–C16)	1.645	π*(C12–C13)	0.389	19.62	0.27	0.07
π(C11–C16)	1.645	π*(C14–C15)	0.387	20.44	0.27	0.07
π(C12–C13)	1.719	π*(C11–C16)	0.403	17.25	0.31	0.07
π(C12–C13)	1.719	π*(C14–C15)	0.387	18.01	0.30	0.07
π(C14–C15)	1.647	π*(C11–C16)	0.403	20.87	0.30	0.07
π(C14–C15)	1.647	π*(C12–C13)	0.389	20.03	0.28	0.07
LP(2)O7	1.874	π*(C1–C2)	0.392	28.39	0.35	0.10
LP(2)O8	1.874	π*(C3–C4)	0.397	29.09	0.35	0.10
LP(2)O17	1.863	π*(C12–C13)	0.389	26.40	0.35	0.09
LP(2)O19	1.863	π*(C14–C15)	0.387	28.82	0.35	0.10

ED(e) is the electron density of donor and acceptor of NBO analysis.
[a] E(2) means the energy of hyper conjugative interactions (stabilization energy).
[b] Energy difference between donor and acceptor i and j NBO orbitals.
[c] F(i,j) is the Fock matrix element between i and j NBO orbitals.

electronegativity, the estimated ionization potential value is relatively high; as a result, the molecule has less of a tendency to receive electrons.

The global hardness of the molecule, proposed by Parr and Pearson [54] encompasses the molecule's reactivity, kinetic stability, and absolute hardness. The molecule possesses higher kinetic stability and reactivity, as evidenced by its global hardness value of 1.929 eV. Chemical softness (0.259 eV) reveals the reactivity of the IRPG drug molecule. Parr et al. [57] anticipated the conception of electrophilicity index [58] to expose the toxicity and reactivity nature [59] of drug molecule and the value for IRPG (3.062 eV) exposes the molecule has low toxicity. These findings demonstrate that the IRPG molecule has good biological activity in terms of pharmacological characteristics and drug design.

3.6. Natural bond orbital's (NBO's)

NBO analysis is used to examine the intra- and intermolecular interactions within the complex, charge transfer, and stabilization energy of molecular systems. The system's stabilisation energy, which is revealed by the delocalization of electron density from Lewis type of NBO's (donor orbital (i)) to virtual Rydberg non-Lewis type of NBO's (acceptor orbital

Table 6. Drug likeness descriptor of IRPG predicted from molinspiration.

Descriptors	Values
Hydrogen Bond Donor (nOHNH)	3
Hydrogen Bond Acceptor (nON)	4
Partition coefficient, Mi logP	2.80
Molecular Weight (MW)	258.27
Topological Polar Surface Area (TPSA) ($Å^2$)	69.92
Number of atoms (natoms)	19
Number of rotatable bonds (nrotb)	3
Number of violations (nviolations)	0
Volume	232.47

Table 7. Bioactivity score of IRPG predicted from molinspiration.

Compound	GPCR ligand	Ion channel modulator	Kinase inhibitor	Nuclear receptor ligand	Protease inhibitor	Enzyme inhibitor
IRPG	-0.13	-0.05	-0.08	0.04	-0.37	0.02

(j)) via second order Fock matrix with hyper conjugative interactions [60] and it can be predictable with the subsequent equation.

$$E(2) = \Delta E_{ij} = \frac{q_i(F_{ij})^2}{\varepsilon_j - \varepsilon_i} \quad (1)$$

Where q_i, F_{ij} and $\varepsilon_{i,j}$ represent the donor orbital occupancy, Fock matrix element between i and j NBO orbitals and orbital energies and diagonal element orbital energies, respectively. The possible interactions for IRPG molecule are π→π* and LP→π* and listed in Table 5. For IRPG molecule the delocalization of π→π* interactions of π(C1–C2) → π*(C3–C4), π(C3–C4) → π*(C5–C6), π(C5–C6) → π*(C1–C2), π(C11–C16) → π*(C14–C15), π(C14–C15) → π*(C11–C16), π(C14–C15) → π*(C12–C13) with high stabilization energy contributions of 26.36, 24.73, 26.28, 20.44, 20.8 and 20.03 kJ/mol respectively. The LP(2) of oxygen atom interacts with π* are LP(2)O7→ π*(C1–C2), LP(2)O8 →π*(C3–C4), LP(2) O17 →π*(C12–C13), LP(2)O19 →π*(C14–C15) and the values are 28.39, 29.09, 26.40 and 28.82 kJ/mol respectively. Moreover, this result shows that IRPG molecule possess high stabilization energy.

3.7. Druglikeness properties

Lipinski's rule of five [61] is formulated by Christopher A. Lipinski to predict the biological activities or pharmacological properties for chemical compound that would make a probable orally drugs in humans. In this work the druglikeness parameters for IRPG molecule were predicted through Molinspiration cheminformatics program (https://www.molinspiration.com). The computed druglikeness values are listed in Table 6. The orally active drugs must obey the following criteria, the H bond donors (OH and NH groups) are not more than 5 (IRPG holds 3), the H bond acceptors (N and O) are not more than 10 (2*5) (IRPG holds 4), the octanol-water partition coefficient or High lipophilicity log p is less than or equal to 5 (IRPG holds 2.80), the molecular weight of the molecule is under 500 g/mol (IRPG holds 258.27 g/mol), van der Waals bumps topological polar surface area is less than 140 $Å^2$ (IRPG holds 69.92 $Å^2$) and number of rotatable bonds is less than 10 (IRPG holds 3) [62]. Hence the molecule IRPG obeys the Lipinski's rule of five, this reveals that the bioavailability is good and it is confirmed as suitable oral drug candidate for humans.

Table 7 shows the predicted bioactivity score for the IRPG molecule based on molinspiration. The probability of bioactivity score for average organic molecules reveals that a value greater than 0.00 indicates that the molecule is active, a value between -0.50 and 0.00 indicates that it is moderately active, and a score less than -0.50 indicates that the molecule is biologically inactive. The nuclear receptor ligand and enzyme inhibitor are 0.04 and 0.02 respectively, confirming that the molecule is active. The GPCR ligand, ion channel modulator, kinase inhibitor and protease inhibitor for IRPG holds -0.13, -0.05, -0.08 and -0.37 respectively, this value reveals that the molecule moderately active. The molecule IRPG is therefore a potential candidate for biological applications and is used for docking analysis because it does not fall under the value less than -0.05 in this result.

Table 8. Prediction of ADMET profiles for IRPG.

ADMET	IRPG
Blood Brain Barrier (BBB+)	0.560014
Human Intestinal Absorption (HIA+, %)	88.446064
Caco-2 cell Permeability (nm/s)	4.89208
Water solubility in buffer (mg/L)	40.1042
Pure water solubility (mg/L)	124.957
Skin permeability (logKp, cm/h)	-3.39671
MDCK cell Permeability (nm/s)	237.503
P-glycoprotein inhibitor	Non-inhibitor
Plasma Protein Binding (PPB, %)	100.0000
CYP 2C19 inhibitor	Inhibitor
CYP 2C9 inhibitor	Inhibitor
CYP 2D6 inhibitor	Non-inhibitor
CYP 2D6 substrate	Non-substrate
CYP 3A4 inhibitor	Non-inhibitor
CYP 3A4 substrate	Non-substrate
Ames test	Mutagen
Ames TA100 (+S9)	Negative
Ames TA100 (-S9)	Negative
Ames TA1535 (+S9)	Negative
Ames TA1535 (-S9)	Negative
Carcinogenicity (Mouse)	Positive
Carcinogenicity (Rat)	Negative
Human Ether-a-go-go-Related Gene (HERG) Inhibition	Medium risk
Lipinski's rule	Suitable
WDI-like rule	Within 90% cutoff
Lead-like rule	Suitable if its binding energy is greater than 0.1microMol
CMC-like rule	Qualified
MDDR-like rule	Mid-structure

3.8. ADMET predictions

Due to the lengthy process at various stages with unexpected failures in drug discovery and high cost, predicting experimental pharmacokinetic and toxicity parameters like absorption, distribution, metabolism, excretion, and toxicity (ADMET) [63, 64] is very risky. In order to save time and money, this ADMET is theoretically predicted using a web-based platform called PreADMET tools (https://preadmet.bmdrc.kr/). Table 8 exposes the theoretically predicted ADMET profiles for IRPG molecule. BBB penetration potential value for IRPG molecule is found to be 0.560014, this indicates that the molecule can cause fewer side effects in the central nervous system. The normal HIA score is between 70 and 100 percent, which indicates excellent intestinal

Table 9. The docking score value of 10 possible conformers of IRPG in the active site of NA enzyme.

Conformers	Binding energy (kcal mol^{-1})	Inhibition constant, ki uM (micromol)	Binding energy (kcal mol^{-1})	Inhibition constant, ki uM (micromol)
1	-5.06	194.57	-6.78	10.66
2	-6.79	10.57	-6.94	8.21
3	-6.13	32.01	-7.31	4.41
4	-5.07	193.77	-6.45	18.65
5	-5.31	129.15	-6.82	9.94
6	-5.70	66.46	-6.32	23.21
7	-5.96	43.03	-6.18	29.57
8	-5.67	69.62	-7.01	7.29
9	-5.82	53.91	-6.57	15.23
10	-5.63	74.35	-5.71	64.91

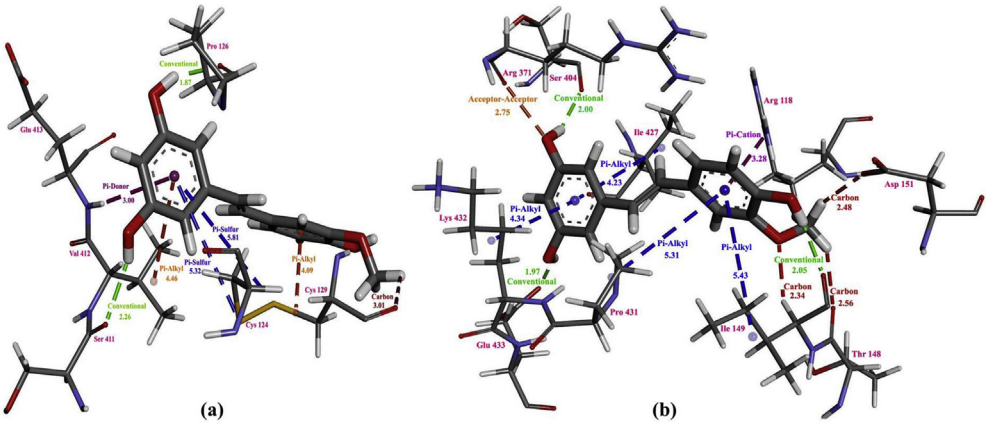

Figure 8. Intermolecular interactions of IRPG with (a) H3N2 NA and (b) H1N1 NA enzyme.

absorption of drug molecules into the bloodstream. In the instance of IRPG, the number was discovered to be 88.446064 percent. IRPG has a skin permeability value of -3.39671 cm/h, indicating that skin is not capable of absorbing the molecule. Caco-2 cell and MDCK cell permeability reveals that oral absorption of drug molecules and the values for IRPG are found to be 4.89208 and 237.503 nm/s respectively, this shows that the molecule is easy to absorb. Higher values have been reached for IRPG's water solubility in buffer and pure water solubility, which are now 40.1042 and 124.957 mg/L, respectively. Ames TA100 (+S9), Ames TA100 (-S9), Ames TA1535 (+S9) and Ames TA1535 (-S9) for all the isomers Ames test is negative therefore it is mutagen. The carcinogenicity for mouse is positive and carcinogenicity for rat is negative for IRPG molecule. In IRPG molecule, HERG inhibition is medium risk, Lipinski's rule is suitable, CMC-like rule is qualified, MDDR-like rule is Mid-structure, Lead-like rule is suitable if its binding energy is greater than 0.1microMol and WDI-like rule is within 90% cutoff. Consequently, the ADMET profiles clearly explain that the IRPG molecule is intermediate candidate for bioactive applications.

3.9. Molecular docking analysis

3.9.1. Ligand preparation

The IRPG 2D structure was created using Chemdraw8.0 software, and it was then transformed into a 3D structure using Chem3D extreme 8.0 tools [65]. Then the compound IRPG was optimized through Gassian09W software using DFT method (basis set 6-311G(d,p)). Additionally, the optimised structure is put into PDB format and used as a ligand. Using the Autodock 4.2 programme, the docking analysis was carried out based on the procedures described in the literature [66].

3.9.2. Protein preparation

The protein structure of H1N1 NA and H3N2 NA enzyme was downloaded from RCSB protein data bank with the PDB id's of 3NSS (1.902 Å resolution) and 2AEP (2.1 Å resolution) respectively. From these proteins, the hetro-atoms such as ligand, ions and water molecules are removed from the H1N1 NA and H3N2 NA enzyme for docking process and taken as a target.

3.9.3. Molecular docking

To assess the drug molecule's typical binding behaviour and activity within the target protein's binding region, a powerful molecular docking computational method is employed. In recent years molecular docking analysis has become a prominent tool in pharmaceutical research. Utilizing Autodock tools, the Kollman charges and polar hydrogen were added to the targets H1N1 NA and H3N2 NA enzyme. For the IRPG molecule Gasteiger charges were added. Autogrid and Autodock are used to create the grid parameter and docking parameter file. The auto grid program was used to generate the affinity (gird) maps of 86 × 86 × 86 Å gird points and 0.375 Å spacing for H1N1 and H3N2 NA enzyme. The *Autogrid.exe* has been used to perform grid parameter. The *Lamarkian*

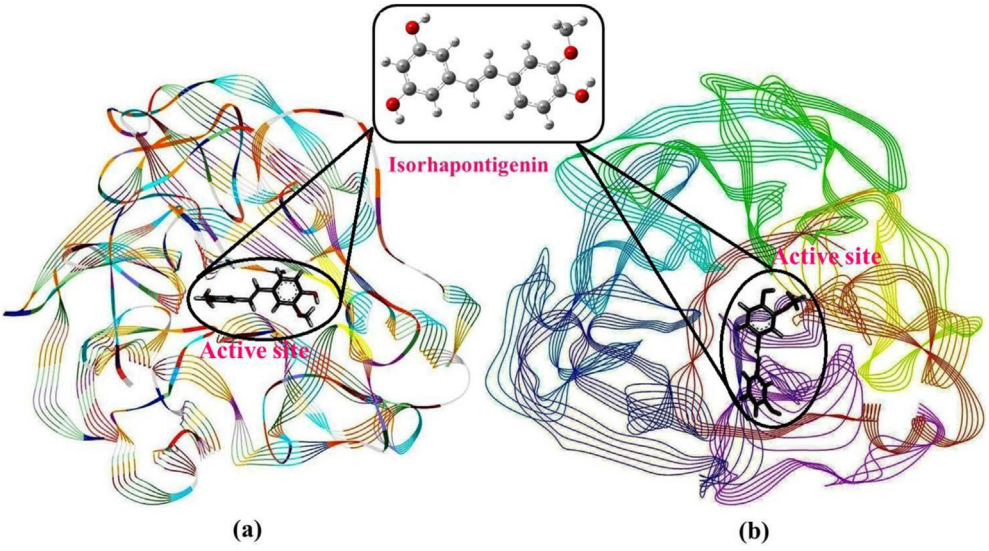

Figure 9. Surface view of IRPG encapsulated in the active site of (a) H3N2 NA and (b) H1N1 NA enzyme.

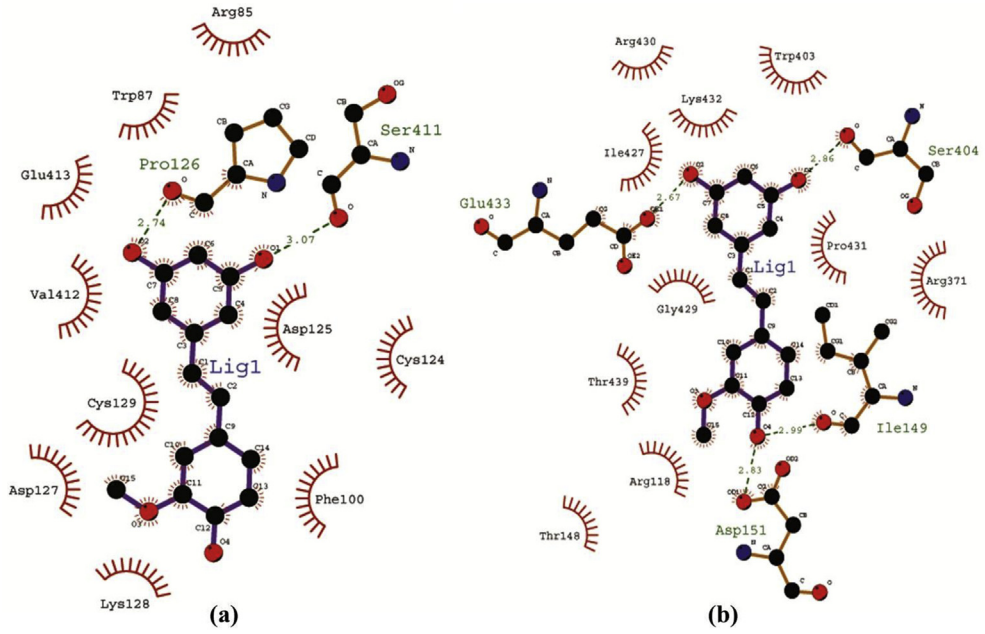

Figure 10. The ligplot showing intermolecular interactions of IRPG in the active site of (a) H3N2 NA and (b) H1N1 NA enzyme.

algorithm was used to perform the conformer searching, whereas the scoring was performed by *Autodock.exe* routine [67, 68]. For exploring the appropriate conformers and scoring the ligand binding, the Generic algorithm and LamarkianGA were employed, respectively. Therefore, the significance of docking process generates 10 conformers and it was represented in Table 9, from these conformers 2nd conformer is the best for H3N2 NA enzyme and 3rd conformer is the best for H1N1 NA enzyme based on lowest binding energy. Moreover, the lowest binding energy values are -6.79 kcal/mol (H3N2 NA) and -7.31 kcal/mol (H1N1 NA) with inhibition constant of 10.57 (H3N2 NA) and 4.41 (H1N1 NA) ki UM (micromol) and this conformer is taken for further process. Likewise, the intermolecular interactions of IRPG with H3N2 NA and H1N1 NA enzyme is analysed through Discovery Studio Visualizer, Chimera, PyMOL and Ligplot and are exposed in Figure 8. Surface view of IRPG molecule embedded in H3N2 NA and H1N1 NA enzyme are shown in Figure 9. Figure 10 shows the Ligplot view of IRPG with H3N2 NA and H1N1 NA enzyme.

The interaction between IRPG with H1N1 NA enzyme reveals the lowest binding energy when compared with H3N2 NA enzyme. In IRPG-H1N1 NA complex the active site residues are Arg 118, Thr 148, Ile 149, Asp 151, Arg 371, Ser 404, Ile 427, Pro 431, Lys 432 and Glu 433. The Ile 149, Ser 404 and Glu 433 residues form strong conventional H bonding interactions with H(23), H(24) and H(33) atoms at a distance of 2.05, 2.00 and 1.97 Å respectively. The Pi-cation and Pi-Alkyl interactions form midst the residues center and ring center. The Pi-cation interactions form in-between Arg 118 residue center and 2nd ring center at a distance of 3.28 Å. Residues Ile 427 and Lys 432 forms Pi-Alkyl interactions with 1st ring center at a distance of 4.23 and 4.34 Å respectively. Residues Ile 149 and Pro 431 also form Pi-Alkyl interactions with 2nd ring center at a distance of 5.43 and 5.31 Å respectively.

In IRPG-H3N2 NA complex the active site residues are Cys 124, Pro 126, Cys 129, Ser 411, Val 412 and Glu 413. The residues Pro 126 and Ser 411 form strong conventional H bonding interactions with H(23) and H(24) atoms at a distance of 1.87 and 2.26 Å respectively. Residues Val 412 and Cys 129 form Pi-Alkyl interaction with 1st and 2nd ring at a distance of 4.46 and 4.09 Å respectively. The Pi-Sulfur interaction form in-between the aromatic ring center and sulphur atom in residues. In IRPG-H3N2 NA complex Pi-sulfur interaction forms between 1st ring and Cys 129 (S) and Cys 124 (S) at a distance of 5.81 and 5.32 Å respectively. The Ligplot also confirms the same active site interactions values for IRPG-H3N2 NA and IRPG-H1N1 NA complexes. This result reveals that IRPG molecule is strongly embedded with H1N1 NA compare with H3N2 NA. Hence this interaction develops the binding affinity of IRPG towards H3N2 NA and H1N1 NA enzymes.

4. Conclusion

The B3LYP/6-311G(d,p) basis set was optimised for the IRPG molecular structure to be in its lowest energy conformation, and the computed parameters are compared with the experimental XRD data pertinent to the structure. The experimental and observed results of FT-IR and FT-Raman are analysed for IRPG molecule. In IRPG molecule the strong bands from HOMO to LUMO level appears in first major contributions of $\pi \rightarrow \pi^*$ transitions with 100%. This transition shows that the IRPG molecule has strong transitions. Mulliken charges and the MEP charges are parallel to IRPG and the map exemplifies that the negative regions are on oxygen atoms while the positive regions are on carbon and hydrogen atoms. These different maps also show the same nature of the IRPG.

The electrophilicity values for IRPG is found to be 3.062 eV, this value confirms that the molecule has less toxicity in nature. IRPG molecule falls under soft molecule category due to low band gap energy value (3.859 eV). The great stability and remarkable chemical selectivity of the IRPG molecule are confirmed by NBO. IRPG molecule obeys the Lipinski's rule of five and bioactivity score values do not fall under the value less than -0.05, therefore the molecule is a potential candidate for bioactive application. An ADMET prediction for IRPG obtains promising biological activity, this prediction helps to improve future drug design. The molecule IRPG enters in the active site cavity of H1N1 and H3N2 NA enzyme, large conformation modification takes place. When compared to IRPG in H3N2 NA enzyme, the H1N1 NA enzyme's IRPG plays a much more significant function and has lower binding energies and inhibition constants. These results suggest that H1N1 NA is a potential inhibitor of influenza A virus and also it provides some key ideas for further development of anti-influenza drugs. These overall results reveal that the molecule IRPG is endorsed in the biological environment.

Declarations

Author contribution statement

Sathya Bangaru: Conceived and designed the experiments; Performed the experiments; Analyzed and interpreted the data; Contributed reagents, materials, analysis tools or data; Wrote the paper.

Govindammal Madhu: Contributed reagents, materials, analysis tools or data.

M. Srinivasan: Performed the experiments.

Prasath Manivannan: Conceived and designed the experiments; Performed the experiments; Analyzed and interpreted the data; Contributed reagents, materials, analysis tools or data; Wrote the paper.

Funding statement

This research did not receive any specific grant from funding agencies in the public, commercial, or not-for-profit sectors.

Data availability statement

No data was used for the research described in the article.

Declaration of interest's statement

The authors declare no conflict of interest.

Additional information

No additional information is available for this paper.

References

[1] Z. Wang, L.P. Cheng, X.H. Zhang, W. Pang, L. Li, J.L. Zhao, Design, synthesis and biological evaluation of novel oseltamivir derivatives as potent neuraminidase inhibitors, Bioorg. Med. Chem. Lett. 27 (2017) 5429–5435.
[2] T.T. Dao, P.H. Nguyen, H.S. Lee, E. Kim, J. Park, S. Il Lim, W.K. Oh, Chalcones as novel influenza A (H1N1) neuraminidase inhibitors from Glycyrrhiza inflata, Bioorg. Med. Chem. Lett. 21 (2011) 294–298.
[3] A. Moscona, Neuraminidase inhibitors for influenza, N. Engl. J. Med. 353 (2005) 1363–1373.
[4] J.S. Oxford, R. Lambkin, A. Elliot, R. Daniels, A. Sefton, D. Gill, Scientific lessons from the first influenza pandemic of the 20th century, Vaccine 24 (2006) 6742–6746.
[5] E. Declercq, J. Neyts, Avian influenza A (H5N1) infection: targets and strategies for chemotherapeutic intervention, Trends Pharmacol. Sci. 28 (2007) 280–285.
[6] A. Flahault, E. Vergu, L. Coudeville, R.F. Grais, Strategies for containing a global influenza pandemic, Vaccine 24 (2006) 6751–6755.
[7] B.A. Goldrick, A.M. Goetz, Pandemic influenza: what infection control professionals should know, Am. J. Infect. Control 35 (2007) 7–13.
[8] C.J. Murray, A.D. Lopez, B. Chin, D. Feehan, K.H. Hill, Estimation of potential global pandemic influenza mortality on the basis of vital registry data from the 1918–20 pandemic: a quantitative analysis, Lancet 368 (2006) 2211–2218.
[9] Z. Zhu, R. Li, G. Xiao, Z. Chen, J. Yang, Q. Zhu, S. Liu, Design, synthesis and structure–activity relationship of novel inhibitors against H5N1 hemagglutinin-mediated membrane fusion, Eur. J. Med. Chem. 57 (2012) 211–216.
[10] R.P. Verma, C. Hansch, A QSAR study on influenza neuraminidase inhibitors, Bioorg. Med. Chem. 14 (2006) 982–996.
[11] J.L. McKimm-Breschkin, S. Barrett, P.A. Pilling, S. Hader, A.G. Watts, V.A. Streltsov, Structural and functional analysis of anti-influenza activity of 4-, 7-, 8- and 9-deoxygenated 2,3-difluoro- N -acetylneuraminic acid derivatives, J. Med. Chem. 61 (2018) 1921–1933.
[12] A. Sakudo, K. Baba, M. Tsukamoto, A. Sugimoto, T. Okada, T. Kobayashi, N. Kawashita, T. Takagi, K. Ikuta, Anionic polymer, poly(methyl vinyl ether–maleic anhydride)-coated beads-based capture of human influenza A and B virus, Bioorg. Med. Chem. 17 (2009) 752–757.
[13] Y. Li, Z. Lin, M. Zhao, T. Xu, C. Wang, L. Hua, H. Wang, H. Xia, B. Zhu, Silver nanoparticle based codelivery of oseltamivir to inhibit the activity of the H1N1 influenza virus through ROS-mediated signaling pathways, ACS Appl. Mater. Interfaces 8 (2016) 24385–24393.
[14] P.C. Nair, M.E. Sobhia, Quantitative structure activity relationship studies on thiourea analogues as influenza virus neuraminidase inhibitors, Eur. J. Med. Chem. 43 (2008) 293–299.
[15] Y. Fang, Y. Yu, Q. Hou, X. Zheng, M. Zhang, D. Zhang, J. Li, X.-R. Wu, C. Huang, The Chinese herb isolate isorhapontigenin induces apoptosis in human cancer cells by down-regulating overexpression of antiapoptotic protein XIAP, J. Biol. Chem. 287 (2012) 35234–35243.
[16] C.-S. Yao, M. Lin, Bioactive stilbene dimers from Gnetum cleistostachyum, Nat. Prod. Res. 19 (2005) 443–448.
[17] U. Grienke, M. Schmidtke, S. von Grafenstein, J. Kirchmair, K.R. Liedl, J.M. Rollinger, Influenza neuraminidase: a druggable target for natural products, Nat. Prod. Rep. 29 (2012) 11–36.
[18] M.J. Frisch, G.W. Trucks, H.B. Schlegel, G.E. Scuseria, M.A. Robb, J.R. Cheeseman, G. Scalmani, V. Barone, B. Mennucci, G.A. Petersson, H. Nakatsuji, M. Caricato, X. Li, H.P. Hratchian, A.F. Izmaylov, J. Bloino, G. Zheng, J.L. Sonnenberg, M. Hada, M. Ehara, K. Toyota, R. Fukuda, J. Hasegawa, M. Ishida, T. Nakajima, Y. Honda, O. Kitao, H. Nakai, T. Vreven, J.A. Montgomery Jr., J.E. Peralta, F. Ogliaro, M. Bearpark, J.J. Heyd, E. Brothers, K.N. Kudin, V.N. Staroverov, T. Keith, R. Kobayashi, J. Normand, K. Raghavachari, A. Rendell, J.C. Burant, S.S. Iyengar, J. Tomasi, M. Cossi, N. Rega, J.M. Millam, M. Klene, J.E. Knox, J.B. Cross, V. Bakken, C. Adamo, J. Jaramillo, R. Gomperts, R.E. Stratmann, O. Yazyev, A.J. Austin, R. Cammi, C. Pomelli, J.W. Ochterski, R.L. Martin, K. Morokuma, V.G. Zakrzewski, G.A. Voth, P. Salvador, J.J. Dannenberg, S. Dapprich, A.D. Daniels, O. Farkas, J.B. Foresman, J.V. Ortiz, J. Cioslowski, D.J. Fox, Gaussian 09, Revision B.01, Gaussian, Gaussian, Inc., Wallingford CT, Gaussian, Inc., Wallingford CT, 2010.
[19] E. Frisch, H.P. Hratchian, R.D. Dennington II, Gaussview, Version 5.0.8, No Title, Gaussian Inc., Wallingford, CT, 2009, p. 235.
[20] M.H. Jamróz, Vibrational energy distribution analysis (VEDA): scopes and limitations, spectrochim, Acta Part A Mol. Biomol. Spectrosc. 114 (2013) 220–230.
[21] A. Stash, V. Tsirelson, WinXPRO : a program for calculating crystal and molecular properties using multipole parameters of the electron density, J. Appl. Crystallogr. 35 (2002) 371–373.
[22] E. Jorge M. Seminario, in: E. Jorge M. Seminario (Ed.), Time-Dependent Density Functional Response Theory for Molecular Systems: Theory, Computational Methods, and Functionals, Elsevier B. V, Amsterdam, 1996.
[23] M.E. Casida, Time-Dependent Density Functional Response Theory for Molecules, 1995, pp. 155–192.
[24] M.A.L. Marques, N.T. Maitra, F.M.S. Nogueira, E.K.U. Gross, A. Rubio (Eds.), Fundamentals of Time-dependent Density Functional Theory, Springer Berlin Heidelberg, Berlin, Heidelberg, 2012.
[25] E.D. Glendening, A.E. Reed, J.E. Carpenter, F. Weinhold. NBO Version 3.1, Gaussian Inc, Pittsburgh, 2003.
[26] G.M. Morris, R. Huey, W. Lindstrom, M.F. Sanner, R.K. Belew, D.S. Goodsell, A.J. Olson, AutoDock4 and AutoDockTools4: automated docking with selective receptor flexibility, J. Comput. Chem. 30 (2009) 2785–2791.
[27] S.D.S. Dassault Syst_emes Biovia, Discovery Studio, DS2016Client32, Dassault Syst_emes, SanDiego, 2016.
[28] E.F. Pettersen, T.D. Goddard, C.C. Huang, G.S. Couch, D.M. Greenblatt, E.C. Meng, T.E. Ferrin, UCSF Chimera?A visualization system for exploratory research and analysis, J. Comput. Chem. 25 (2004) 1605–1612.
[29] W.L. DeLano, The PyMOL Molecular Graphics System, Schrödinger LLC, 2002. Wwwpymolorg, Version 1, http://www.pymol.org.
[30] R.A. Laskowski, M.B. Swindells, LigPlot+: multiple ligand–protein interaction diagrams for drug discovery, J. Chem. Inf. Model. 51 (2011) 2778–2786.
[31] F. Ahmad, A. Mahmood, T. Muhmood, Machine learning-integrated omics for the risk and safety assessment of nanomaterials, Biomater. Sci. 9 (2021) 1598–1608.
[32] A. Mahmood, J.-L. Wang, A time and resource efficient machine learning assisted design of non-fullerene small molecule acceptors for P3HT-based organic solar cells and green solvent selection, J. Mater. Chem. A. 9 (2021) 15684–15695.
[33] A. Mahmood, A. Irfan, J. Wang, Developing efficient small molecule acceptors with sp 2 hybridized nitrogen at different positions by density functional theory calculations, molecular dynamics simulations and machine learning, Chem. Eur J. (2021).
[34] R.G. Parr, W. Yang, in: Density Funct. Theory Atoms Mol., Oxford University Press, New York, NY, 1989.
[35] J.K. Labanowski, J.W. Andzelm (Eds.), Density Functional Methods in Chemistry, Springer, New York, NY, 1991.
[36] B. Zarychta, C.G. Gianopoulos, A.A. Pinkerton, Revised structure of trans-resveratrol: implications for its proposed antioxidant mechanism, Bioorg. Med. Chem. Lett. 26 (2016) 1416–1418.
[37] R.I. Zubatyuk, O.V. Shishkin, L. Gorb, J. Leszczynski, Homonuclear versus heteronuclear resonance-assisted hydrogen bonds: tautomerism, aromaticity, and intramolecular hydrogen bonding in heterocyclic systems with different exocyclic proton donor/acceptor, J. Phys. Chem. 113 (2009) 2943–2952.
[38] Russell D. Johnson III (Ed.), NIST Comput. Chem. Comp. Benchmark Database, Release, 2018.
[39] A. Pielesz, D. Biniaś, J. Wieczorek, FT-IR spectroscopic analysis in monitoring of hydroxyl stretching vibrations in plant hydrogels, Polim. Med. 41 (2011) 33–42. http://www.ncbi.nlm.nih.gov/pubmed/22332324.
[40] K. Bhavani, S. Renuga, S. Muthu, K. Sankara narayanan, Quantum mechanical study and spectroscopic (FT-IR, FT-Raman, 13C, 1H) study, first order hyperpolarizability, NBO analysis, HOMO and LUMO analysis of 2-acetoxybenzoic acid by density functional methods, Spectrochim. Acta Part A Mol. Biomol. Spectrosc. 136 (2015) 1260–1268.
[41] L.J. Bellamy, The Infra-red Spectra of Complex Molecules, Springer Netherlands, Dordrecht, 1975.
[42] P.S. Kalsi, Spectroscopy of Organic Compounds, New Age International Publishers, 2002.
[43] G. Chalasinski, M.M. Szczesniak, Origins of structure and energetics of van der Waals clusters from ab initio calculations, Chem. Rev. 94 (1994) 1723–1765.

[44] S. Muthu, M. Prasath, R. Arun Balaji, Experimental and theoretical investigations of spectroscopic properties of 8-chloro-1-methyl-6-phenyl-4H-[1,2,4]triazolo[4,3-a][1,4]benzodiazepine, Spectrochim, Acta Part A Mol. Biomol. Spectrosc. 106 (2013) 129–145.
[45] A. Choperena, P. Painter, An infrared spectroscopic study of hydrogen bonding in ethyl phenol: a model system for polymer phenolics, Vib. Spectrosc. 51 (2009) 110–118.
[46] P. Politzer, J.S. Murray, The fundamental nature and role of the electrostatic potential in atoms and molecules, Theor. Chem. Accounts Theor. Comput. Model. 108 (2002) 134–142.
[47] J.S.M.K. Sen, Molecular electrostatic potentials: concepts and applications, in: Mol. Electrost. Potentials Concepts Appl., Elsevier B, Amsterdam, 1996.
[48] E. Scrocco, J. Tomasi, Electronic Molecular Structure, Reactivity and Intermolecular Forces: an Euristic Interpretation by Means of Electrostatic Molecular Potentials, 1978, pp. 115–193.
[49] S. Bangaru, P. Manivannan, Probing the structural properties, binding mode and intermolecular interactions of herbacetin against H1N1 neuraminidase using vibrational spectroscopic, quantum chemical calculation and molecular docking studies, Res. Chem. Intermed. 47 (2021) 2775–2799.
[50] S. Bangaru, P. Manivannan, S. Muthu, Spectroscopic investigations, quantum chemical calculations and molecular docking studies of Mangiferin - an anti-viral agent of H1N1 Influenza virus, Chem. Data Collect. 30 (2020), 100580.
[51] B. Sathya, S. Karthi, K. Ajaijawahar, M. Prasath, Probing the vibrational spectroscopic properties and binding mechanism of anti-influenza agent Liquiritin using experimental and computational studies, Res. Chem. Intermed. 46 (2020) 4475–4507.
[52] B. Sathya, M. Prasath, Spectroscopic (FT-IR, FT-Raman, UV–Vis), quantum chemical calculation and molecular docking evaluation of liquiritigenin: an influenza A (H1N1) neuraminidase inhibitor, Res. Chem. Intermed. 45 (2019) 2135–2166.
[53] T. Koopmans, Über die Zuordnung von Wellenfunktionen und Eigenwerten zu den Einzelnen Elektronen Eines Atoms, Physica 1 (1934) 104–113.
[54] R.G. Parr, R.G. Pearson, Absolute hardness: companion parameter to absolute electronegativity, J. Am. Chem. Soc. 105 (1983) 7512–7516.
[55] R.S. Mulliken, Electronic population analysis on LCAO–MO molecular wave functions. I, J. Chem. Phys. 23 (1955) 1833–1840.
[56] L. Pauling, G.W. Wheland, The nature of the chemical bond. V, J. Chem. Phys. 2 (1934) 482.
[57] R.G. Parr, L.V. Szentpály, S. Liu, Electrophilicity index, J. Am. Chem. Soc. 121 (1999) 1922–1924.
[58] B. Sathya, M. Prasath, M. Selvapandiyan, K. Prabha, Vibrational analysis (FT-IR and FT-Raman spectra) and molecular docking evaluation of MPTB in GABA receptor, J. Cluster Sci. 30 (2019) 1025–1035.
[59] D.R. Roy, U. Sarkar, P.K. Chattaraj, A. Mitra, J. Padmanabhan, R. Parthasarathi, V. Subramanian, S. Van Damme, P. Bultinck, Analyzing toxicity through electrophilicity, Mol. Divers. 10 (2006) 119–131.
[60] C.R.L.F. Weinhold, Valency and bonding: a natural bond orbital donor acceptor perspective, in: Val. Bond. A Nat. Bond Orbital Donor Accept. Perspect., Cambridge University Press, Cambridge, Cambridge, 2005.
[61] C.A. Lipinski, F. Lombardo, B.W. Dominy, P.J. Feeney, Experimental and computational approaches to estimate solubility and permeability in drug discovery and development settings 1PII of original article: S0169-409X(96)00423-1. The article was originally published in Advanced Drug Delivery Reviews 23 (1997), Adv. Drug Deliv. Rev. 46 (2001) 3–26.
[62] E.A. Alodeani, M. Arshad, M.A. Izhari, Anti-uropathogenic activity, drug likeness, physicochemical and molecular docking assessment of (E-)-N′-(substituted-benzylidene)-2-(quinolin-8-yloxy) acetohydrazide, Asian Pac. J. Trop. Biomed. 5 (2015) 676–683.
[63] L. Di, H. Kerns Edward, Drug-Like Properties: concepts, structure design, and methods from ADME to toxicity optimization, 2nd edition, Elsevier, 2016, pp. 1–580.
[64] C. Kramer, A. Ting, H. Zheng, J. Hert, T. Schindler, M. Stahl, G. Robb, J.J. Crawford, J. Blaney, S. Montague, A.G. Leach, A.G. Dossetter, E.J. Griffen, Learning medicinal chemistry absorption, distribution, metabolism, excretion, and toxicity (ADMET) rules from cross-company matched molecular pairs analysis (MMPA), J. Med. Chem. 61 (2018) 3277–3292.
[65] L.D. Mendelsohn, ChemDraw 8 ultra, windows and macintosh Versions, J. Chem. Inf. Comput. Sci. 44 (2004) 2225–2226.
[66] M.H.S.M.D. Rizvi, S. Shakil, A simple click by click protocol to perform docking: AutoDock 4.2 made easy for non-bioinformaticians, EXCLI. J. 12 (2013) 831–857.
[67] M.F. Nazar, M.I. Abdullah, A. Badshah, A. Mahmood, U.A. Rana, S.U.-D. Khan, Synthesis, structure–activity relationship and molecular docking of cyclohexenone based analogous as potent non-nucleoside reverse-transcriptase inhibitors, J. Mol. Struct. 1086 (2015) 8–16.
[68] M.I. Abdullah, A. Mahmood, M. Madni, S. Masood, M. Kashif, Synthesis, characterization, theoretical, anti-bacterial and molecular docking studies of quinoline based chalcones as a DNA gyrase inhibitor, Bioorg. Chem. 54 (2014) 31–37.